ACSNANO

www.acsnano.org

ARTICLE

Epitaxial Templating of Two-Dimensional Metal Chloride Nanocrystals on Monolayer Molybdenum Disulfide

Shanshan Wang,[†] Huashan Li,[‡] Junying Zhang,[§] Shaoqiang Guo,[§] Wenshuo Xu,[†] Jeffrey C. Grossman,[‡] and Jamie H. Warner*[,†]

[†]Department of Materials, University of Oxford, Parks Road, Oxford OX1 3PH, United Kingdom

[‡]Department of Materials Science and Engineering, Massachusetts Institute of Technology, 77 Massachusetts Avenue, Cambridge, Massachusetts 02139, United States

[§]Key Laboratory of Micro-nano Measurement, Manipulation and Physics (Ministry of Education), Department of Physics, Beihang University, Beijing 100191, P.R. China

S *Supporting Information*

ABSTRACT: **We demonstrate the formation of ionic metal chloride (CuCl) two-dimensional (2D) nanocrystals epitaxially templated on the surface of monolayer molybdenum disulfide (MoS_2). These 2D CuCl nanocrystals are single atomic planes from a nonlayered bulk CuCl structure. They are stabilized as a 2D monolayer on the surface of the MoS_2 through interactions with the uniform periodic surface of the MoS_2. The heterostructure 2D system is studied at the atomic level using aberration-corrected transmission electron microscopy at 80 kV. Dynamics of discrete rotations of the CuCl nanocrystals are observed, maintaining two types of preferential alignments to the MoS_2 lattice, confirming that the strong interlayer interactions drive the stable CuCl structure. Strain maps are produced from displacement maps and used to track real-time variations of local atomic bonding and defect production. Density functional theory calculations interpret the formation of two types of energetically advantageous commensurate superlattices *via* strong chemical bonds at interfaces and predict their corresponding electronic structures. These results show how vertical heterostructured 2D nanoscale systems can be formed beyond the simple assembly of preformed layered materials and provide indications about how different 2D components and their interfacial coupling mode could influence the overall property of the heterostructures.**

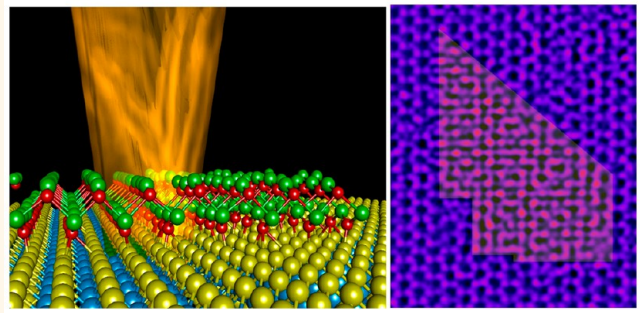

KEYWORDS: *MoS_2, 2D crystal, metal chloride, vertical heterostructure, AC-TEM, epitaxy*

The successful isolation of individual graphene layers sparked a surge in the exploration of other 2D crystals, such as hexagonal boron nitride (h-BN) and transition metal dichalcogenides (MoS_2, WS_2, *etc.*).[1−5] With the enrichment of various kinds of 2D materials, interest has been extended to the artificial assembly of different atomically thin layers to form van der Waals heterostructures.[6] To date, typical vertical layered heterostructures (VLHs), including graphene/h-BN,[7,8] MoS_2/graphene,[9−11] MoS_2/h-BN,[12,13] and MoS_2/WS_2,[14−16] have been fabricated through either sequential mechanical transfer or direct growth using chemical vapor deposition (CVD). The 2D building blocks are generally layered atomic crystals in bulk form with strong covalent bonds in-plane and weak interlayer van der Waals interactions, which facilitates the isolation into monolayer films and then the vertical stacking into hybrid 2D heterostructures. The interlayer interactions in VLHs depend not only on the two materials but also on the relative orientation of the lattice directions in each layer. Lattice alignment between neighboring 2D crystals forms heteroepitaxial bilayers with surface reconstruction, interfacial charge transfer, and proximity effects such as Coulomb interactions and quantum tunneling.[17−22] Yang *et al.* showed the epitaxial growth of single-domain graphene on h-BN using a plasma-assisted deposition approach, which induced a second Dirac point to appear.[17] Gong *et al.* reported the synthesis of epitaxially stacked WS_2/MoS_2 heterostructures by a vapor phase growth at high temperature (~850 °C), which generated

Received: April 25, 2017
Accepted: May 25, 2017
Published: June 12, 2017

DOI: 10.1021/acsnano.7b02838
ACS Nano 2017, 11, 6404−6415

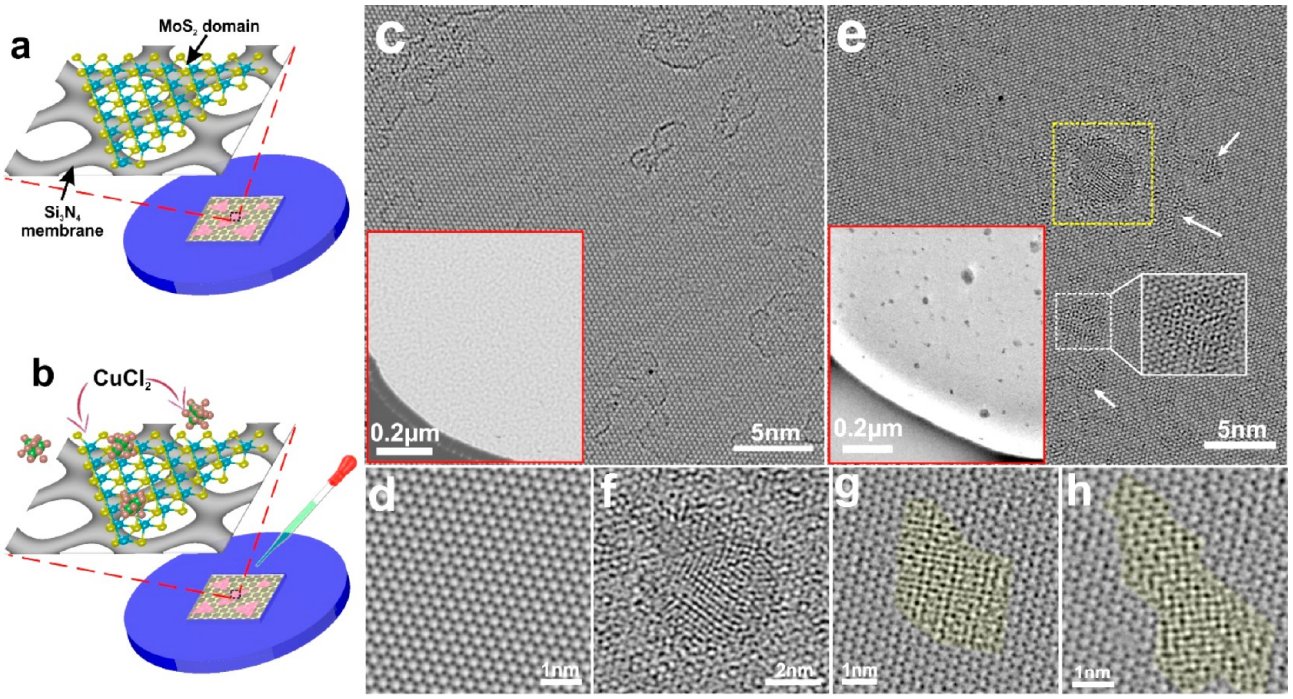

Figure 1. (a,b) Schematic illustrations showing the transfer of monolayer MoS_2 onto the Si_3N_4 TEM grid (a) followed by doping MoS_2 films with copper(II) chloride ($CuCl_2$) solution through a drop-casting procedure (b). (c) Medium-magnification AC-TEM image of a pristine monolayer MoS_2 film before $CuCl_2$ deposition. Inset is the low-magnification AC-TEM image of the same area. (d) High-magnification AC-TEM image of intrinsic MoS_2 monolayers. (e) Medium-magnification AC-TEM image of a pristine monolayer MoS_2 film doped by $CuCl_2$, where exotic nanocrystals (yellow dashed box) with thin amorphous substances surrounding (white dashed box and white arrows) can be seen on the surface. Inset on the left bottom box is the low-magnification TEM image of the same area showing the attachment of small nanoparticles on the MoS_2 surface. (f) Magnified AC-TEM image of the yellow boxed region in (e). (g,h) High-magnification AC-TEM images showing cubic 2D CuCl nanocrystals grown on monolayer MoS_2 with two typical preferential orientations after electron beam irradiation (white dashed box and white arrows in (e)). Different moiré patterns are seen, as highlighted by semitransparent yellow masks, indicating various lattice correlations between 2D CuCl and single-layer MoS_2 lattice points.

a strong interlayer exciton transition due to the type-II band alignment.[14]

The ability to extend vertical heterostructures by using materials that are not typically layered systems would further expand the variety of options for material choice and ultimately control over the desired properties. Recent research using aberration-corrected (scanning) transmission electron microscopy (AC-(S)TEM) has shown that a 2D material template can help the stabilization and crystallization of nonlayered materials into a 2D form. Chen *et al.* showed the epitaxial growth of 2D crystalline gold nanocrystals on graphene at elevated temperatures.[23] Al Balushi *et al.* reported the growth of 2D gallium nitride (GaN) on the bulk 6H-SiC substrate with the help of graphene encapsulation.[24] However, the achievement of 2D nonlayered materials is still lacking with limited understanding about the interfacial interactions between the 2D layered and nonlayered material. In addition, they commonly adopt a similar crystal symmetry in the stacking plane, making it little known whether nonlayered materials having a different lattice symmetry from the layered template can also be stabilized in a 2D form. Recently, 2D suspended Fe within graphene nanopores and 2D layered ZnO nanocrystals on graphene have been produced.[25,26] Moreover, expanding the underlying 2D template beyond graphene, such as using monolayer transition metal dichalcogenides, is highly desirable, which would provide opportunities to create exotic mixed 2D hybrid semiconductor systems with distinct fundamental physics.

Metal chlorides offer a wide range of compounds and have been frequently used to dope graphene in the form of $FeCl_2$ to lower its sheet resistance for electronic applications, indicating strong interactions with the hexagonal 2D lattice structure. However, semiconducting metal chlorides are more promising for VLHs with monolayer TMDs due to possibility of forming heterostructures with distinct excitonic states. CuCl is a I−VII compound with ionic character and adopts a wide direct band gap, similar in energy to GaN and ZnO. The cubic zinc blende structure is the most thermodynamically preferable and commonly seen form with a wide direct band gap of 3.4 eV[27] and a large exciton binding energy (190 meV for the Z_3 exciton) (Supporting Information Figure S1).[28] It comprises two interpenetrating face-centered cubic (fcc) unit cells occupied by Cu and Cl, which can be seen as a binary diamond crystal structure. For a CuCl crystal, which is in one-unit-cell thickness, it possesses only four atomic layers with each atomic column having only one atom, either Cu or Cl, from the view along [001] direction (note that atoms sitting at the top and bottom faces of the unit cell can only be considered as half an atom because they need to be shared with neighbors). It also has a large dipole moment, because Cu and Cl atoms with opposite charges are arranged in different atomic layers stacked alternatively. Since 2D CuCl and monolayer MoS_2 are seen as the analogue of diamond and graphene, respectively, fabricating 2D CuCl on monolayer MoS_2 will realize the achievement of "diamond-graphene-like" 2D vertical heterostructures, in which two 2D building blocks possess distinct and

DOI: 10.1021/acsnano.7b02838
ACS Nano 2017, 11, 6404−6415

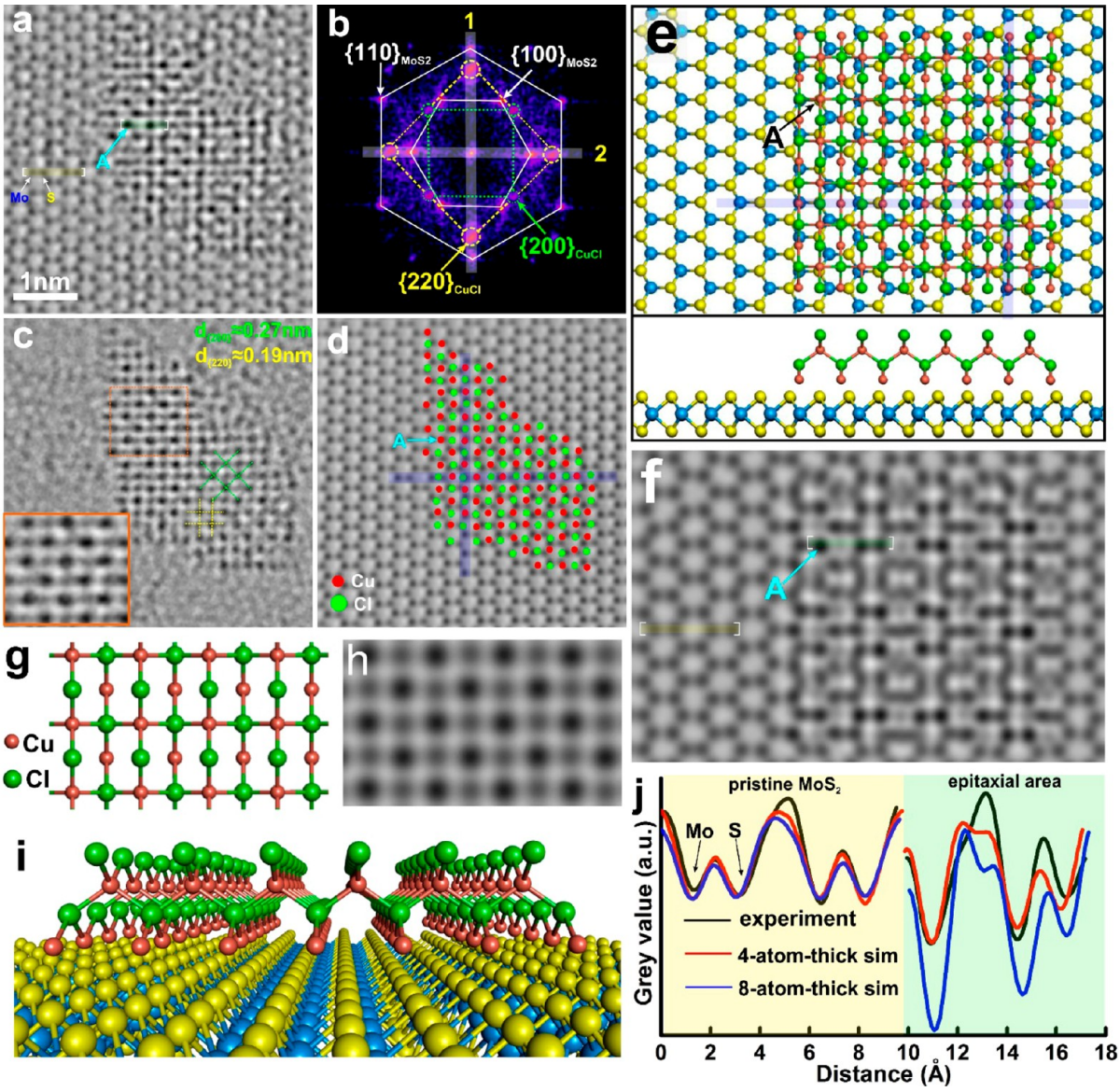

Figure 2. (a) AC-TEM image showing a typical example of 2D cubic CuCl on monolayer MoS_2 with type-I relative heteroepitaxy. (b) Two-dimensional FFT of (a). Aligned spots between CuCl and MoS_2 are marked by two half-transparent white lines, 1 and 2, respectively. (c) Reconstructed AC-TEM image after applying a mask to 2D FFT of (b) to remove the MoS_2 lattice contribution, showing only the 2D CuCl lattice structure. Inset is the magnified image of the orange boxed region. Yellow and green dashed lines label the lattice planes of {200} and {220} of this 2D CuCl nanocrystal, respectively. (d) Image showing the atomic positions of the Cu and Cl atoms relative to the monolayer MoS_2 template (see Methods). Purple lines indicate two different lattice plane directions belonging to $\{220\}_{CuCl}$ are aligned with one zigzag and one armchair direction of monolayer MoS_2, respectively. (e) Atomic model based on the analysis from (b) and (d), shown in top view that represents the projection seen by AC-TEM. Two purple lines indicate the two main lattice alignment relationship between 2D CuCl and MoS_2. The side view is placed in the bottom part. Blue, yellow, red and green spheres represent Mo, S, Cu and Cl atoms, respectively. The model of 2D CuCl is from its intrinsic bulk counterparts. (f) Multislice TEM image simulation based on the atomic model in (e). (g) Isolated 2D CuCl model after removing the bottom monolayer MoS_2 lattice in (e). (h) Multislice TEM image simulation based on (g). (i) Three-dimensional perspective side view of the model in (e) showing the CuCl structure. (j) Line profiles comparing the atomic column intensities from the experimental and simulated images (see Methods).

typical crystal symmetries. The generation of this vertical heterostructure will provide fundamental knowledge to help expand the library of 2D materials further and understand the evolution of the overall properties after coupling different 2D blocks together.

Here, we show that monolayer 2D CuCl nanocrystals can easily form on the surface of monolayer MoS_2. The CuCl phase observed is a bulk 3D material, not a layered system, and its formation into a monolayer sheet is driven by the underlying epitaxial interactions with the MoS_2. These CuCl 2D crystals are formed *in situ* within an AC-TEM, by electron beam decomposition of solution-deposited $CuCl_2$ precursor material that resides on the surface of MoS_2. Two preferred epitaxial orientations of 2D CuCl on monolayer MoS_2 have been observed with density functional theory (DFT)-relaxed models showing the detailed coupling mode at the interface. We image the atomic positions of the CuCl atoms within the nanocrystals to accurately determine the crystal structure and also track the real-time dynamics of CuCl nanocrystals as they undergo phase changes and rotations, providing insights into the epitaxial

DOI: 10.1021/acsnano.7b02838
ACS Nano 2017, 11, 6404–6415

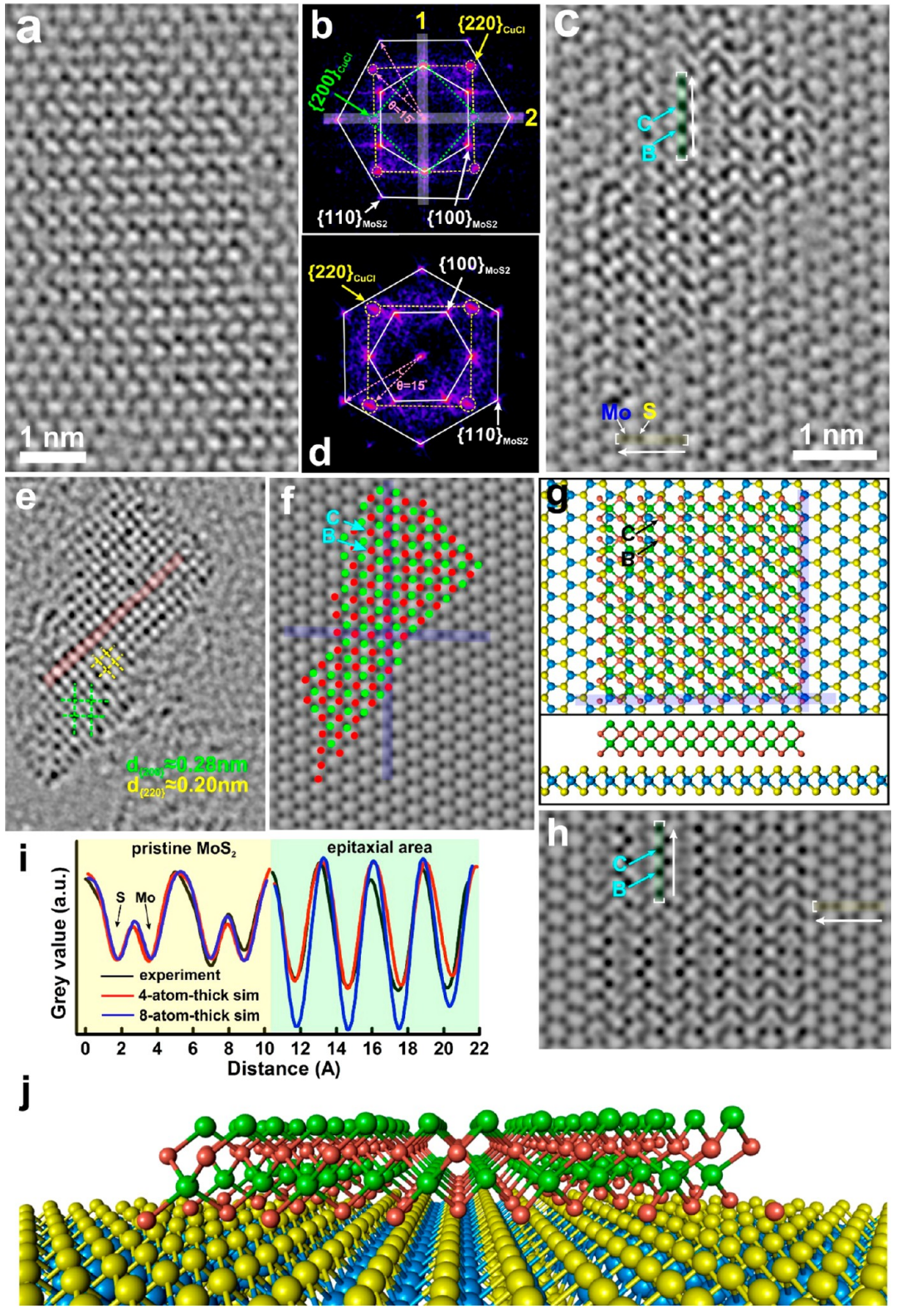

Figure 3. (a) AC-TEM image of one typical example of type-II heteroepitaxy mode between 2D CuCl and monolayer MoS_2. (b) Two-dimensional FFT of (a). (c) AC-TEM image of another typical example of type-II heteroepitaxy mode captured at a different defocus from that of (a). (d) Two-dimensional FFT of (c). (e) Reconstructed AC-TEM image after applying a mask to (d) to filter out MoS_2 lattice contribution. (f) Image showing the atomic positions of Cu and Cl atoms from CuCl relative to the monolayer MoS_2 template. Purple lines indicate that two different lattice plane directions belonging to $\{200\}_{CuCl}$ are aligned with one zigzag and one armchair direction of monolayer MoS_2. (g) Atomic model based on the analysis from (d) and (f) with both the projective (top panel) and side (bottom panel) view. (h) Multislice TEM image simulation corresponding to the atomic model in (g). (i) Line profiles comparing the atomic column intensities from the experimental and simulated images (see Method). (j) Three-dimensional perspective side view of the model in (g).

DOI: 10.1021/acsnano.7b02838
ACS Nano 2017, 11, 6404−6415

correlations to the underlying MoS_2 lattice. The 2D displacement and strain maps are generated to quantitatively investigate the lattice distortion in 2D CuCl nanocrystals. The electronic structure of two types of heteroepitaxial structures of CuCl/MoS_2 are provided by DFT calculations, indicating that both electronic and spintronic properties may be substantially affected by the orbital hybridization *via* chemical bonding and intrinsic dipole moment in CuCl nanocrystals.

RESULTS AND DISCUSSION

Monolayer MoS_2 was synthesized by chemical vapor deposition (CVD) method similar to previous work and transferred to Si_3N_4 TEM grids with 2 μm holes (Figure 1a).[28] Both the low-magnification and high-resolution TEM images confirm the clean MoS_2 surface with only small regions covered by typical amorphous carbon residue (Figure 1c). The AC-TEM image in Figure 1d shows the hexagonal lattice structure of pristine monolayer MoS_2 with atomic resolution. One drop of 0.05 M copper(II) chloride ($CuCl_2$) in ethanol solution was deposited onto MoS_2 (Figure 1b) and allowed to dry in air, leading to the formation of nanoparticles with diameters of several nanometers on the MoS_2 surface (Figure 1e). The large three-dimensional nanocrystals (Figure 1f) are easily observed during AC-TEM, but examination of the area also revealed thin amorphous $CuCl_2$ material was present, with contrast lower than that of the larger nanocrystals. Electron beam irradiation of the amorphous $CuCl_2$ region resulted in the transformation to a crystalline phase (Supporting Information Figure S19). Characterization of the crystalline structure revealed they are predominantly 2D copper(I) chloride (CuCl) nanocrystals in the cubic zinc blende structure. The CuCl nanocrystals adopt epitaxial orientations with the underlying monolayer MoS_2 (Figure 1g,h and Supporting Information Figures S2−S9).

Figure 2a shows the AC-TEM image of 2D cubic zinc blende CuCl on MoS_2 in a "type-I" heteroepitaxial orientation that results in a specific moiré pattern. The 2D fast Fourier transform (FFT) of Figure 2a shows four sets of spots: two sets which are in hexagonal pattern can be assigned to {100} and {110} of monolayer MoS_2, representing zigzag and armchair directions, respectively, whereas the other two sets which are in the squared pattern belong to {200} and {220} of 2D CuCl. According to the CuCl lattice configuration, {220} of CuCl ($\{220\}_{CuCl}$) adopts two different crystal directions, which are perpendicular to each other (orange dashed lines in Supporting Information Figure S1c). One crystal direction of $\{220\}_{CuCl}$ is aligned with one armchair direction of MoS_2, whereas the other lattice plane orientation of $\{220\}_{CuCl}$ is parallel to one zigzag direction of MoS_2, as indicated by two semitransparent white columns in Figure 2b. This crystallographic relationship between heteroepitaxial 2D CuCl and the template monolayer MoS_2 can be defined as $(001)_{CuCl}//(001)_{MoS_2}$; $[110]_{CuCl}//[110]_{MoS_2}$. The lattice structure of 2D CuCl can be extracted by applying a mask to the 2D FFT to filter out the lattice contribution from monolayer MoS_2 (Figure 2c). The 2D CuCl has a squared lattice periodicity from the projective view with dark and bright spots arranged alternatively, indicating its thickness to be the integral multiples of four atomic layers, equaling to one-unit-cell thickness of the bulk CuCl crystal (Supporting Information Figure S10). The interplanar spacings of $\{200\}_{CuCl}$ and $\{220\}_{CuCl}$ are measured to be ~0.27 and ~0.19 nm, respectively, which is consistent with that for bulk CuCl (Supporting Information Figure S1e). The *d*-spacing of $\{200\}_{CuCl}$ has a good match with that of $\{100\}_{MoS_2}$, which may contribute to the formation and stability of this heteroepitaxial structure. Figure 2d shows the absolute location for each Cu and Cl atom from 2D CuCl on the monolayer MoS_2 lattice in real space, which confirms the crystal plane alignment relation based on the 2D FFT in Figure 2b. For the construction of the atomic model for type-I CuCl/MoS_2 heterostructures, a point where the Cu atom from 2D CuCl and the double S atoms from monolayer MoS_2 are almost perfectly eclipsed was found in Figure 2d, marked as "A". It is chosen as a reference point to determine the absolute position between the 2D CuCl atomic model and the monolayer MoS_2 model, thus obtaining the atomic model shown in Figure 2e. The 3D perspective view of the model (Figure 2i) highlights the nonplanar configuration of 2D cubic CuCl lattice. The multislice TEM simulation generated based on this atomic model agrees with the AC-TEM image and shows a "brick-wall-like" moiré pattern at the epitaxial region (Figure 2f) similar to the AC-TEM image (Figure 2a). We also did the TEM image simulation based on the individual 2D CuCl atomic model (Figure 2g), which provides a similar squared lattice configuration in the top view, agreeing well with the reconstructed AC-TEM image of CuCl (inset of Figure 2c). To determine the thickness of CuCl, we compared the relative intensity variations between monolayer MoS_2 and the typical structures in the heteroepitaxial regions for both the experimental AC-TEM image and the image simulations with different 2D CuCl thickness (Figure 2i). It is confirmed that the CuCl is only four atoms thick (equaling to one-unit-cell thick in bulk CuCl) having only one atom, either Cu or Cl, in each atomic column from the projection view (Figure 2e).

Figure 3a shows an AC-TEM of the type-II heteroepitaxy between 2D CuCl and monolayer MoS_2. The 2D FFT shows that two different crystal directions of $\{200\}_{CuCl}$, which are perpendicular to each other, are aligned to one zigzag and one armchair orientation of MoS_2, respectively, as indicated by two white semitransparent lines in Figure 3b. The crystallographic relation for this type-II heteroepitaxy can be expressed as $(001)_{CuCl}//(001)_{MoS_2}$; $[100]_{CuCl}//[110]_{MoS_2}$. Since the interplanar spacings of $\{200\}_{CuCl}$ and $\{100\}_{MoS_2}$ are very close, two reflexes covered by line "1", which correspond to the crystal planes from $\{200\}_{CuCl}$ and $\{100\}_{MoS_2}$, respectively, overlap with each other. According to the geometric relations between the cubic CuCl and hexagonal MoS_2 lattice, the smallest intersection angle between two crystal faces from $\{220\}_{CuCl}$ and $\{110\}_{MoS_2}$ is 15° in the type-II heteroepitaxy, as marked by the angle θ between two pink arrows in Figure 3b.

Figure 3c is another typical example of type-II heteroepitaxy but is captured at a different defocus. This results in the low visibility of reflexes corresponding to $\{200\}_{CuCl}$ (Figure 3d). However, we are still able to determine the stacking orientation between CuCl and MoS_2 by measuring θ and confirm this epitaxial mode to be also type-II. The 2D CuCl crystal is individually shown in Figure 3e after the signal contribution from the MoS_2 lattice is removed. The atom contrast between two neighboring atomic positions is more uniform compared with that in Figure 2c, without a distinct light and dark alternation in brightness. This may arise from a different defocus value for the 2D CuCl lattice under this imaging condition, which also results in a decreased intensity of $\{200\}_{CuCl}$ reflexes in 2D FFT (Figure 3d and Supporting

DOI: 10.1021/acsnano.7b02838
ACS Nano 2017, 11, 6404−6415

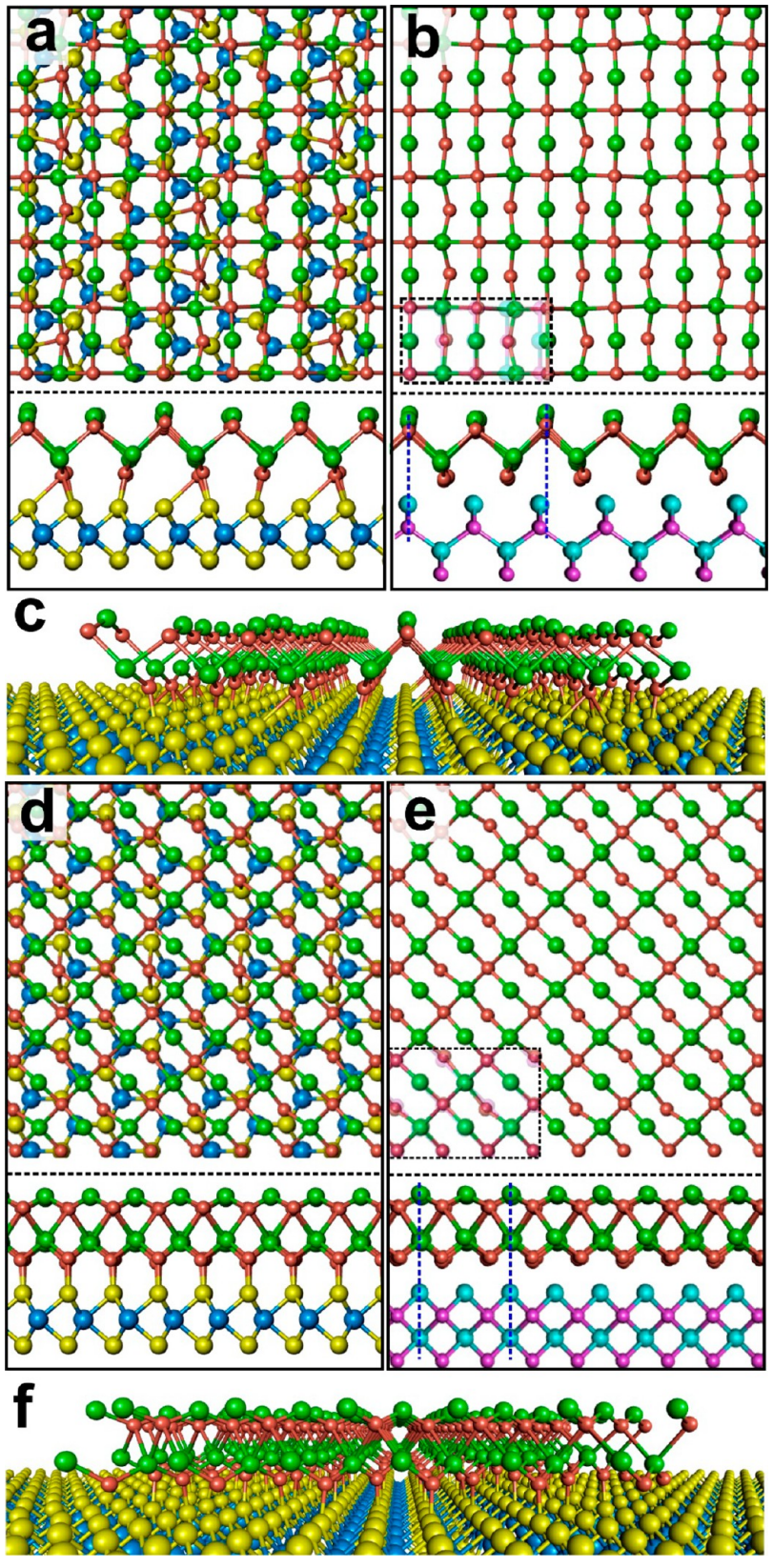

Figure 4. DFT-relaxed atomic model of type-I (a) and type-II (d) $CuCl/MoS_2$ heterostructures with both the projective view and the side view. The monolayer MoS_2 template is removed to show the four-atom-thick CuCl atomic model separately in type-I (b) and type-II (e) heteroepitaxy. The unrelaxed cubic zinc blende CuCl atomic model, having Cu and Cl atoms colored in pink and cyan, respectively, is placed at the bottom of the side view, which is used as a comparison to show the lattice distortion before and after the DFT relaxation. The dashed black box in the top panel of (b) and (e) overlaps a semitransparent unrelaxed CuCl model on the DFT-relaxed one to show the structural deformation of CuCl in the projection view. The 3D perspective views of type-I (c) and type-II (f) $CuCl/MoS_2$ heterostructures are also provided.

DOI: 10.1021/acsnano.7b02838
ACS Nano 2017, 11, 6404−6415

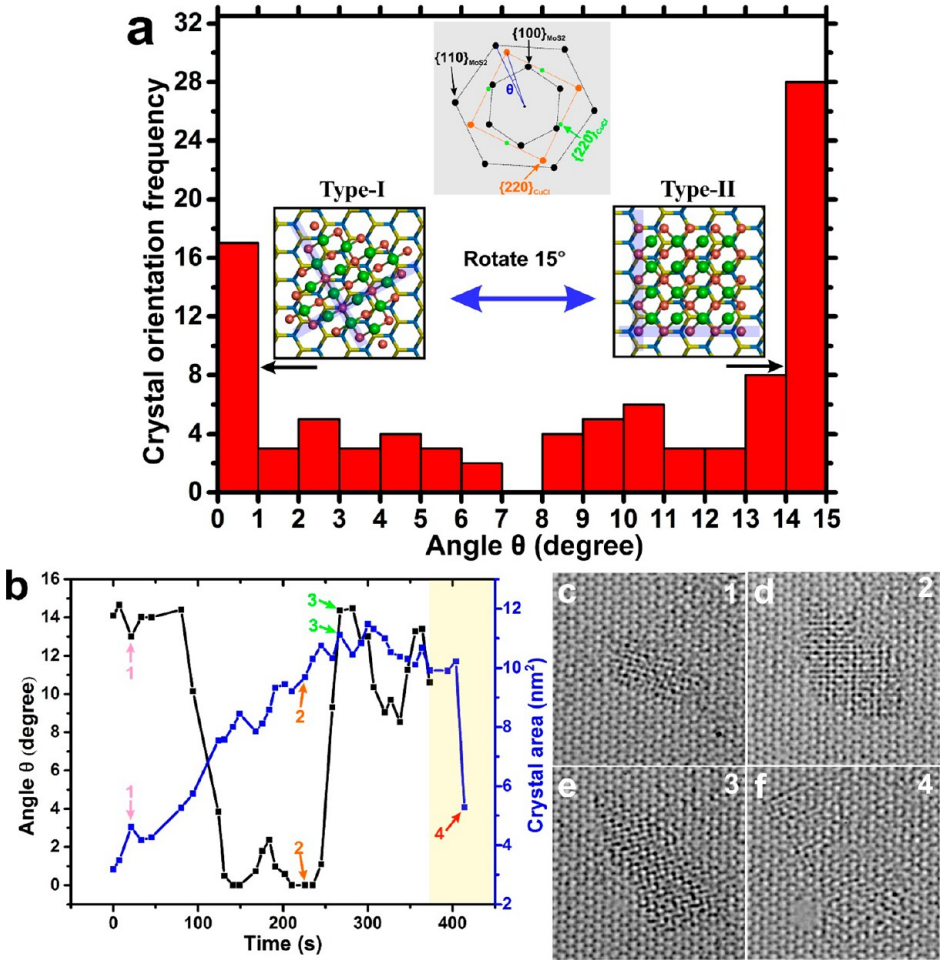

Figure 5. (a) Histograms showing the distribution of stacking orientation between 2D CuCl crystals and the monolayer MoS_2 template. (b) Plots showing the stacking orientation (black curve) and the area (blue curve) changes of one 2D CuCl crystal as a function of the exposure time under the electron beam. The yellow region indicates the time period when CuCl began to degrade. (c–f) Time series of AC-TEM images showing this 2D CuCl crystal at four different time points, as marked by numbers 1 to 4 in (b). Figure 4d,e is the same as Figures 2a and 3c.

Information Figure S11). The interplanar spacing for $\{220\}_{CuCl}$ is measured to be ~0.20 nm by using reflexes from monolayer MoS_2 in 2D FFT as the reference. Therefore, we can deduce the *d*-spacing of $\{200\}_{CuCl}$ to be approximately 0.28 nm based on the CuCl crystal structure. The lattice parameters for 2D CuCl in type-I and type-II heteroepitaxial modes show a good consistency with each other with a small error, which could derive from either measurements or tiny TEM image distortion. An obvious increase on the structural disorder, revealed as the lattice distortion marked by a red strip in Figure 3e, can be observed in the 2D CuCl crystal. Such loss of structural coherence will be quantitatively analyzed by generating 2D strain maps in Figure 6. The positions of each atom from 2D CuCl on monolayer MoS_2 are shown in Figure 3f, demonstrating the crystal direction alignment between two perpendicular orientations from $\{200\}_{CuCl}$ and the MoS_2 zigzag and armchair directions, as highlighted by two purple lines. The atomic model is generated in Figure 3g from the view angle along the yellow arrow in Figure 3c. The corresponding multislice TEM simulation (Figure 3h) exhibits the same "leaf-like" moiré pattern as the experimental image (Figure 3c). The intensity line profiles between the pristine monolayer MoS_2 and the typical epitaxial region for both the experimental image and the simulations confirms the four-atom thickness of the 2D CuCl crystal in this example, which is consistent with type-I $CuCl/MoS_2$ heterostructures.

DFT calculations were conducted to achieve the relaxed atomic model of $CuCl/MoS_2$ heterostructures in type-I and type-II epitaxy (Figure 4). The monolayer MoS_2 and the four-atom-thick CuCl layer are mainly coupled *via* the strong Cu–S chemical bonding rather than weak van der Waals interactions due to a high reactivity of unsaturated Cu atoms at the interface. This indicates that there exists a strict requirement about the position matching between Cu and S atoms in 2D $CuCl/MoS_2$ to enable a periodic bonding pattern for the establishment of the commensurate superlattice. This is different to previously studied 2D van der Waals hetero-structures, which have a high tolerance on the lattice mismatch at the interface. Since monolayer MoS_2 has higher rigidity than 2D CuCl, it triggers a substantial lattice distortion in CuCl with MoS_2 barely perturbed. It is found that the 2D CuCl can adopt several equivalent or energetically similar structures at such a symmetric interface, and the energy barrier for the structure transition from one to another is low. Given the intrinsic flexibility of 2D CuCl and the energy injected by the electron beam, the atomic configuration of 2D CuCl may oscillate between different configurations during AC-TEM imaging. Therefore, the periodic square lattice in the projective view we

DOI: 10.1021/acsnano.7b02838
ACS Nano 2017, 11, 6404–6415

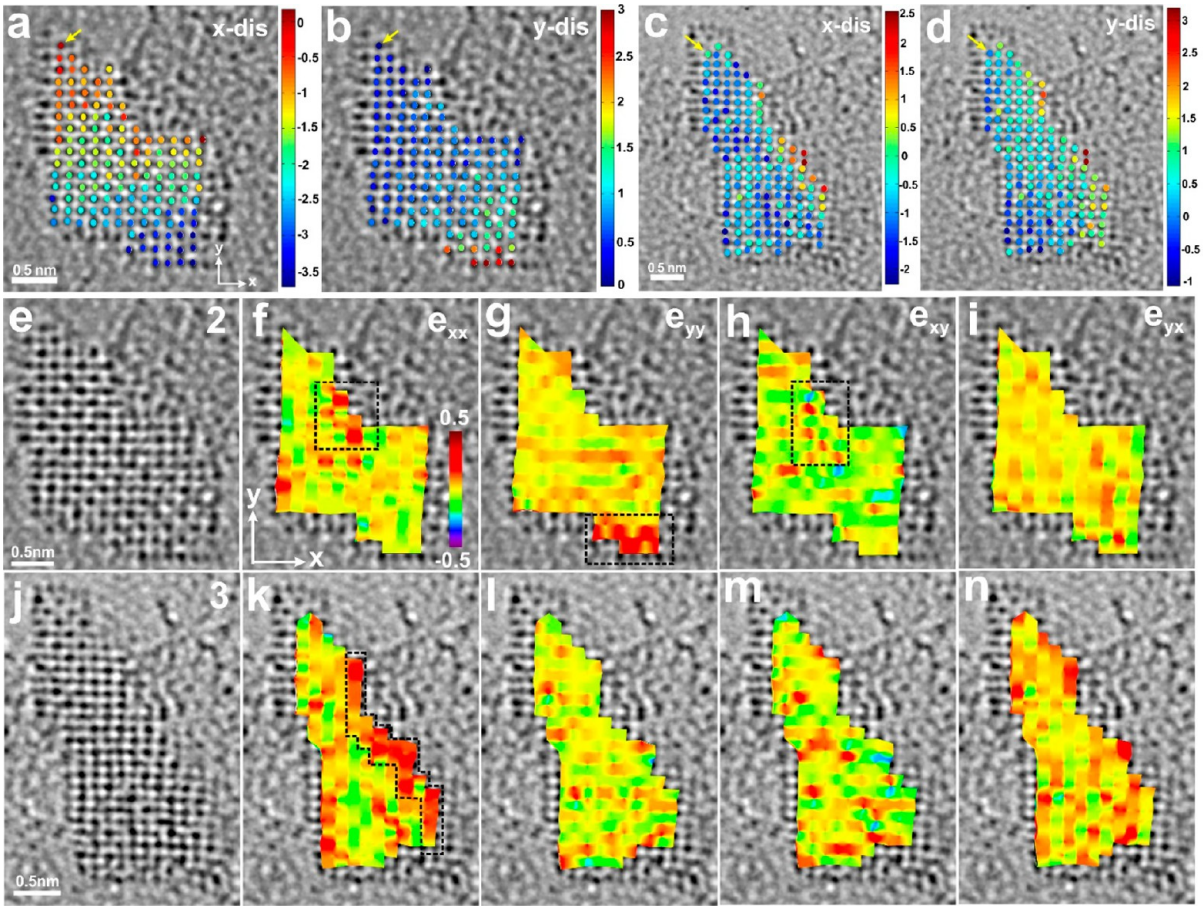

Figure 6. (a,b) Two-dimensional displacement maps in the *x* and *y* direction for the 2D CuCl nanocrystal in (e). (c,d) Two-dimensional displacement maps in the *x* and *y* direction for the 2D CuCl nanocrystal in (j). The unit of all color bars for displacement maps is Å. (e) Reconstructed AC-TEM image in Figure 5d showing the lattice structure of individual 2D CuCl nanocrystal at time point 2 after filtering out the signal contribution from monolayer MoS_2 lattice. The heteroepitaxial model between CuCl and MoS_2 is type-I. (f–i) Two-dimensional strain maps of $\partial U_x/\partial x$, $\partial U_y/\partial y$, $\partial U_x/\partial y$, and $\partial U_y/\partial x$ for 2D CuCl nanocrystal in (e). The color scale is ±0.5. (j) Reconstructed AC-TEM image in Figure 5e showing the individual 2D CuCl nanocrystal at time point 3. The heteroepitaxial model between CuCl and MoS_2 is type-II. (k–n) Two-dimensional strain maps of $\partial U_x/\partial x$, $\partial U_y/\partial y$, $\partial U_x/\partial y$, and $\partial U_y/\partial x$ for 2D CuCl nanocrystal in (j). The color scale is ±0.5.

observed in a AC-TEM image integrated over a single exposure (1–2 s) may be a time-averaged structure of 2D CuCl. This phenomenon also occurred in the TEM observation of the monovacancy in graphene.[29] We averaged over two DFT-relaxed equivalent structures with opposite in-plane polarized directions for type-I and type-II heteroepitaxy, respectively, and obtained the final averaged atomic configurations (Figure 4a,d and Supporting Information Figure S12) with their corresponding 3D perspective views (Figure 4c,f). After the bottom monolayer MoS_2 was removed, the separate 2D CuCl structure could be seen (Figure 4b,e), which preserves the square lattice geometry in the projective view well, consistent with the experimental observations, with slight in-plane distortion and a minor change on the lateral lattice spacing. The lattice deformation predominantly occurs in the direction perpendicular to the 2D membrane, as depicted by the side-view comparison between DFT-relaxed and unrelaxed CuCl atomic models in Figure 4b,e. The intensity line profiles between experimental AC-TEM images and image simulations based on corresponding averaged DFT-relaxed type-I and type-II heteroepitaxy models agree well with each other, indicating the validity of our deduction on the lattice configuration (Supporting Information Figures S13 and S14). Despite the distinct stacking patterns and lattice mismatches (Supporting Information Table S1), DFT calculations show that these two types of $CuCl/MoS_2$ interfaces have similar binding energies (type I, 0.47 eV; type II, 0.43 eV per unit of CuCl), which supports the hypothesis that the coupling between materials is primarily through chemical bonding rather than van der Waals forces. In addition, the interface structure is extremely sensitive to the choice of the supercell. Even a small deviation from the ideal situation leads to a significant amount of Cu–Cl bonds breaking and the ruin of the squared projective lattice structure (Supporting Information Figure S15). This further implies that the formation of an ordered cubic hexagonal interface relies on stringent material matching.

The stacking orientation distribution of 2D cubic CuCl on monolayer MoS_2 was investigated by analyzing the 2D FFT of more than 90 different AC-TEM frames (Figure 5a). As the schematic illustration of a typical 2D FFT of one $CuCl/MoS_2$ TEM image shown on the top panel of Figure 5a, we use the smallest intersection angle (θ) between one crystal direction of $\{220\}_{CuCl}$ and its closest one MoS_2 armchair direction to describe the stacking orientation between two films. Based on the symmetry relation between cubic CuCl and hexagonal MoS_2 crystals, two types of heteroepitaxial modes can transform to each other by rotating 15° (Supporting Information Figure S16). Therefore, type-I heteroepitaxy

DOI: 10.1021/acsnano.7b02838
ACS Nano 2017, 11, 6404–6415

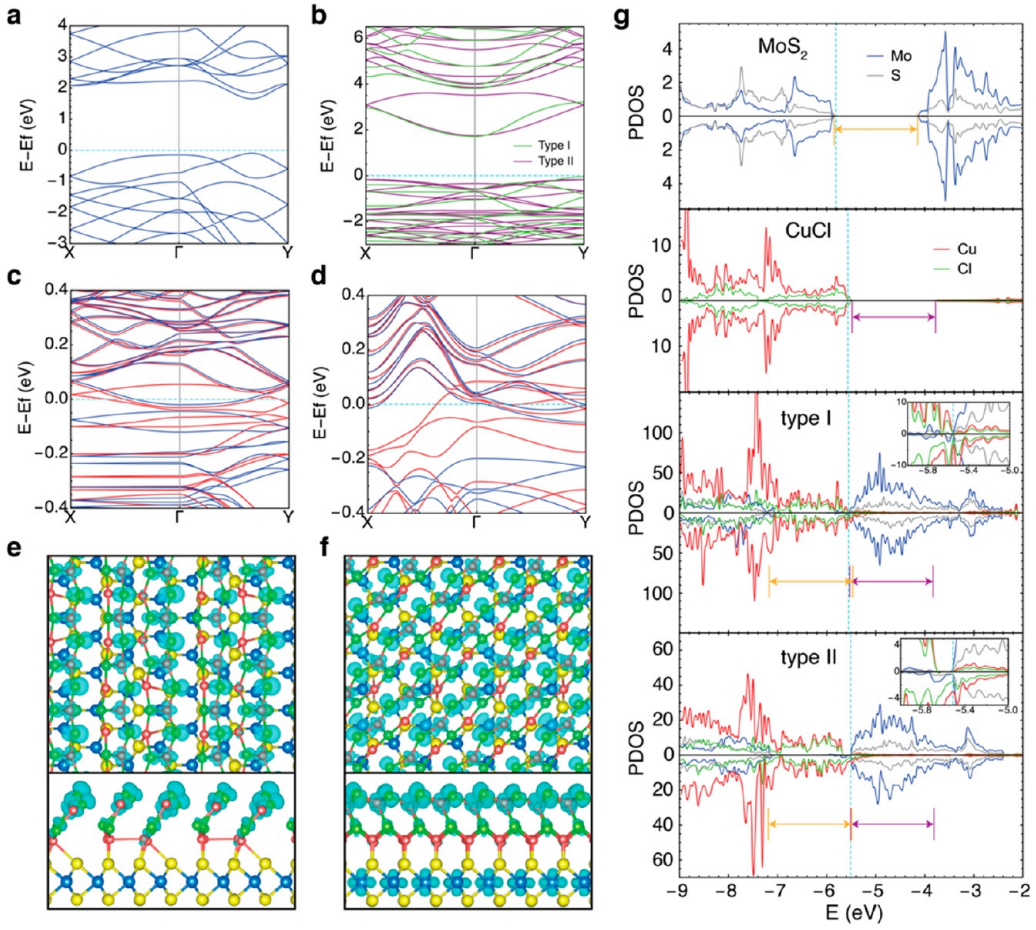

Figure 7. Electronic properties of MoS_2/CuCl heterostructures predicted by DFT simulations. Band structures of (a) isolated MoS_2 monolayer, (b) isolated CuCl monolayer with type I and type II alignments, (c) type I and (d) type II MoS_2/CuCl heterostructures, with the Fermi level illustrated by the dashed cyan lines. (c) Spin-up and (d) spin-down components are shown in blue and red, respectively. Partial charge densities of the highest valence bands at Γ point for the (e) type-I and (f) type-II interfaces. (g) PDOS on elements for the isolated MoS_2 monolayer, isolated CuCl monolayer, and two types of MoS_2/CuCl heterostructures. The orange and purple arrows present the band gaps of the MoS_2 and CuCl monolayers and their energy shifts in the presence of the interfaces. The insets show the PDOS around the Fermi levels, which highlight the emergence of midgap states.

corresponds to $\theta = 0°$, whereas type-II heteroepitaxy corresponds to $\theta = 15°$. All the other stacking modes can be expressed by θ between 0 and 15°. By tracking one CuCl crystal from its birth to death, we found that it can rotate under the electron beam irradiation (Figure 5b) with approximately 50% of its lifetime adopting either type-I ($0° \leq \theta \leq 1°$) or type-II ($14° \leq \theta \leq 15°$) stacking orientations with respect to the MoS_2 template. This agrees with the statistical results in Figure 5a, where type-I and type-II heteroepitaxy yield a percentage of 18 and 30%, respectively, indicating an energetic preference for the crystal alignment strategy of these two epitaxial modes. Such epitaxial tendency between 2D CuCl and monolayer MoS_2 disappeared as CuCl nanocrystals became thicker, which might be induced by the reduced interfacial interactions of the template monolayer MoS_2 to the above CuCl (Supporting Information Figure S17). The blue curve in Figure 5b shows the area changes of the same 2D CuCl nanocrystal as a function of the observation time under the electron beam, which reveals the formation dynamics and the stability of this ultrathin metal chloride nanocrystal. The formation of 2D CuCl starts from a small nucleation under the electron beam illumination and then increases its area steadily followed by a level-off, which finally ends up with a sharp degradation. The lifespan of this CuCl under the electron beam illumination is more than 6 min, indicating a relatively high stability of this 2D metal chloride nanocrystal templated on monolayer MoS_2 (Supporting Information Figure S20). Four AC-TEM images showing this 2D CuCl crystal at different stages are exhibited in Figure 5c–f.

As depicted in Figure 3e, we observed an obvious structural disorder for 2D cubic zinc blende CuCl nanocrystals compared with the intrinsic atomic model for its bulk counterparts. This increased structural incoherence is quantitatively studied by calculating the 2D strain field in the CuCl lattice. Figure 6e,j shows two reconstructed AC-TEM images based on Figure 5d,e showing 2D CuCl nanocrystals alone after filtering out the monolayer MoS_2 lattice. The heteroepitaxial model between 2D CuCl and the monolayer MoS_2 template in Figure 6e,j belongs to type-I and type-II, respectively. We examined the strain in these two 2D CuCl nanocrystals (Figure 6f–i and Figure 6k–n) from the displacement maps obtained by resolving the displacement values for each atom in the real space (Figure 6a–d; see Methods). It shows that the lattice periodicity of these ultrathin CuCl nanocrystals decreases with an increased level of random distortion in the lattice and a broader distribution of bond length, as indicated by the 2D normal and shear strain maps in Figure 6. Such an increase of the structural disorder

DOI: 10.1021/acsnano.7b02838
ACS Nano 2017, 11, 6404–6415

matches well with the DFT-calculated atomic models for 2D CuCl in both two types of heteroepitaxy (Figure 4b,e). The lattice irregularity could be triggered by the monolayer MoS_2 template, which adopts a different crystal symmetry compared with the 2D cubic zinc blende CuCl nanocrystal. In addition, the high flexibility of ultrathin CuCl membrane and the strong chemical bonding at the CuCl/MoS_2 interface may further promote the structural disorder in 2D CuCl nanocrystals. It was also found that atoms close to edges and corners of 2D CuCl sometimes suffer higher strains compared with the body region (black dashed boxes in Figure 6f–h Figure 6k), which might be due to diverse unsatisfied bonding environments at edges and corners and can drive an increased inhomogeneous internal strain.

DFT+U method was employed to qualitatively explore the electronic properties of the two types of favorable MoS_2/CuCl heterostructures identified by experiments. Whereas the bulk MoS_2 and CuCl crystals have indirect and direct band gaps, respectively, the inhomogeneous quantum confinement effects in momentum space turn their monolayer counterparts to be direct and indirect band gap material. As expected from their different symmetry groups, the isolated MoS_2 and CuCl monolayers exhibit distinct dispersion relationships with the band edges located at the K and Γ/Y points (Figure 7a,b), implying that the assistance of phonons is required for the charge transfer between these two domains. In contrast to the type-II interface speculated from the energy levels of individual components, the projected density of states (PDOS) of the combined MoS_2/CuCl systems suggest a type-III alignment with metallic behaviors (Figure 7g). This can be explained by the noticeable shifts of MoS_2 energy levels in the presence of a large dipole moment embedded in the adjacent CuCl crystal, as well as the emergence of additional midgap states originating from the strong orbital hybridization between chemically connected sheets. The consequential internal charge transfer from CuCl to MoS_2 in combination with the potential gradient modify the occupations of d-orbitals and lead to the splitting between spin-up and spin-down states (Figure 7c,d). Due to the ionic nature and flexibility of CuCl crystals, the wave functions remain delocalized over the entire sheets, even though there exist noticeable distortions at the interface (Figure 7e,f and Supporting Information Figure S18). From the similar PDOS obtained at the two types of interfaces, both energy level alignment and ground-state charge distribution are insensitive to the stacking pattern. However, the dynamic processes such as charge hopping, optical excitation, and exciton dissociation may intensively rely on the crystalline alignment because electron couplings between the two sheets are sensitive to the wave function overlap at the interface, and the tunneling probabilities depend on the alignment in momentum space.

CONCLUSION

In summary, we showed that 2D ionic CuCl crystals adopt a nonlayered cubic zinc blende crystal configuration on the surface of the MoS_2 monolayers with strong epitaxial correlations between the lattice directions of the two crystals. The generation of 2D CuCl was achieved by simply depositing the $CuCl_2$ solution onto MoS_2 followed by a proper dose of electron beam irradiation to initiate precursor decomposition and subsequent *in situ* reactivity. The 2D strain maps on the CuCl membrane show a decrease of lattice periodicity as the bulk CuCl is thinned into a 2D form and templated on the substrate with different symmetry. DFT simulations explained the formation of commensurate superlattices *via* bonding pattern matching and revealed the distinct electronic structures of the MoS_2/CuCl heterostructures compared to their components. These studies provide insights into the generation of more 2D heterostructures with a broader material choice and show how 2D transition metal dichalcogenides perform as a template to stabilize the nonlayered ionic crystal membrane on top through interfacial interactions.

METHODS

Synthesis and Transfer of MoS_2 Monolayers. Monolayer MoS_2 was grown directly on the SiO_2/Si (300 nm thick SiO_2) substrate by a hydrogen-free chemical vapor deposition method under atmospheric pressure, which is similar to that in previously reported work.[12,30] Molybdenum trioxide (MoO_3, ≥99.5%, Sigma-Aldrich) and sulfur (S, ≥99.5%, Sigma-Aldrich) powder were used as precursors. We loaded MoO_3 powder into a smaller diameter tube (∼1 cm) and placed S powder in the outer 1 in. quartz tube, as this will avoid the cross-contamination between two precursors at high temperature. Two furnaces were applied to provide independent temperature control for both precursors and the substrate. S powder and the substrate were put in the center of the first and second furnace, while MoO_3 powder was positioned at the upstream of the second furnace. The whole growth system was first flushed by the argon gas using a high flow rate for 40 min followed by preintroducing S vapor for ∼15 min to create a sulfur-sufficient atmosphere. After that, the temperature for the second furnace started to increase to ∼800 °C at a ramping rate of 40 °C/min and was maintained for 15 min under 150 sccm argon flow. The argon flow rate was then reduced to 10 sccm and kept for 25 min before the growth stopped, followed by a fast cooling process. The temperature for S was retained at ∼180 °C during the whole synthesis period.

A thin film of poly(methyl methacrylate) (PMMA) was spin-coated onto the surface of the MoS_2/SiO_2/Si substrate. The underlying SiO_2 was etched away by floating it on the 1 mol/L potassium hydroxide solution. After it peeled off, the PMMA/MoS_2 membrane was transferred into the deionized water for three times to wash off residual contamination from the etchant. The film was subsequently scooped up by a quantifoil TEM grid (Agar Scientific AGS175-3). Once left to dry in the air for overnight, the sample was baked on a hot plate at 150 °C for 15 min to ensure a strong interfacial attachment between MoS_2 monolayers and the quantifoil membrane. Finally, the TEM grid was submerged in acetone for 8 h to remove the PMMA scaffold.

Transmission Electron Microscopy and Image Processing. The AC-TEM was conducted using Oxford's JEOL JEM-2200MCO field emission gun TEM with a CEOS imaging aberration corrector under a low accelerating voltage of 80 kV. AC-TEM images were captured using a Gatan Ultrascan 4k × 4k CCD camera with 1–2 s acquisition time and 2 pixel binning under the electron dose of ∼10^5 e^-/nm^2. The pixel resolution for high-magnification AC-TEM images is 145 pixels/nm. ImageJ software was applied to process AC-TEM images. Images were initially adjusted with a band-pass filter (between 100 and 1 pixel) to modify the long-range nonuniformity on the illumination intensity and then smoothed by applying a Gaussian blur (2–4 pixels). Atomic models were generated using the Accelrys Discovery Studio Visualizer software. Simulated multislice images based on corresponding atomic models were established *via* JEMS software with a proper parameter adjustment according to the TEM experimental condition. The reconstructed AC-TEM images shown in Figure 2d are constructed by first applying a mask to 2D FFT in Figure 2b to only choose the lattice contribution from MoS_2 and obtaining the reconstructed AC-TEM image. Second, we overlap Figure 2c, which only includes a 2D CuCl lattice, onto this reconstructed AC-TEM having only MoS_2 lattice structure and use red and green circles to label Cu and Cl atomic positions in Figure 2c. Third, we remove Figure 2c to get the image in Figure 2d, where the position of each atom in the 2D CuCl crystal with respect to the MoS_2 substrate is clearly revealed. Figure 3f is obtained using the same method. For the line profile in Figure 2i, the intensity at the pristine and heteroepitaxial

DOI: 10.1021/acsnano.7b02838
ACS Nano 2017, 11, 6404–6415

regions are measured along semitransparent yellow and cyan lines in experimental and simulated TEM images, respectively. The atomic column marked as "A" in Figure 2a,f corresponds to the lattice structure where the Cu atom from CuCl almost fully overlaps with a double S atoms of monolayer MoS_2, which is confirmed by the analysis in Figure 2d and the atomic model in Figure 2e. It is chosen as a starting point for the intensity measurement in the heteroepitaxial area because the lattice stacking pattern between CuCl and monolayer MoS_2 around this point has a good correspondence between AC-TEM image and the image simulation. Therefore, only the thickness of 2D CuCl influences the match of intensity line profiles between the experimental and simulated image. In Figure 3i, a similar approach is used, where two reference points, B and C, are selected.

Two-Dimensional Displacement and Strain Maps. The generation of 2D strain maps in Figure 5 is realized by using a similar real space analysis method as previously reported work.[31−34] It is based on the generation of 2D displacement maps. We first identified the precise positions of atoms in the 2D CuCl based on the reconstructed AC-TEM images in Figure 6e,j and then subtracted them from their expected locations in a regular and periodic 2D CuCl lattice. The interplanar spacing of this regular and periodic lattice is set to be the average interplanar spacing of the 2D CuCl nanocrystal in Figure 6e,j, respectively, confirmed by the 2D FFT of corresponding AC-TEM images. After getting the displacement maps of 2D CuCl crystals, we can resolve the 2D local lattice strain by first doing the scattered interpolant on the displacement map with a proper step size and then calculating the displacement value difference divided by their location variations along certain directions between each two interpolated spots to form 2D gradient maps of $\partial Ux/\partial x$, $\partial Uy/\partial y$, $\partial Ux/\partial y$, and $\partial Uy/\partial x$. These strain maps could not only show the general lattice distortion but also reveal the level of the structural regularity at different locations in a single 2D CuCl nanocrystal formed on monolayer MoS_2, such as comparing the variations on the bond length or the lattice shear between atomic sites in the crystal center and close to edges.

Density Functional Theory Calculation. Standard *ab initio* calculations within the framework of density functional theory were performed to investigate the microscopic structures and electronic properties of MoS_2/CuCl heterostructures, using the Vienna Ab Initio Simulation Package (VASP v5.4).[35] Plane-wave and projector-augmented wave-type pseudopotentials[36] were used, with GGA-PBE exchange-correlation functional[37] and a 400 eV kinetic-energy cutoff. The DFT-D3 method of Grimme[38] was employed to take the van der Waals interactions into account, with the cutoff radius for pair interactions set to 50 Å. Dipole correction[39] was included to correct the leading errors caused by the large dipole moment in a finite periodic simulation box. A 15 Å vacuum was constructed to avoid fake interactions between periodic images. The structures were relaxed until all forces were smaller than 0.02 eV/Å. For both favorable alignment types identified by experiments, a range of supercells with relatively small lattice mismatches were tested, and the candidates with the highest regularities (type I, MoS_2-3 × 5, CuCl-4 × 4, 154 atoms; type II, MoS_2-1 × 7, CuCl-1 × 4, 74 atoms) were selected as representatives to explore the electronic properties. The average structures of the nearly degenerate representatives induced by symmetry were used for TEM image simulations. The electronic structures were computed with Monkhorst−Pack k-point grids[40] of 9 × 9 × 1 and 21 × 6 × 1 for the two types of heterostructures, respectively. DFT+U method was employed to enhance the electronic correlation,[41] with U = 8 eV and J = 0.95 eV applied to the Cu d-orbitals to correct the energy level of Cu-d band.[42] We note that given the incapability of DFT to account for many-body effects, the results should be interpreted qualitatively for revealing the impact of heterostructure on electronic properties.

ASSOCIATED CONTENT

Supporting Information

The Supporting Information is available free of charge on the ACS Publications website at DOI: 10.1021/acsnano.7b02838.

Supplementary figures including atomic models of different possible crystal structures containing Cu on monolayer MoS_2, TEM image simulations showing the cubic CuCl with different atomic thickness, the influence of defocus values on the imaging of cubic CuCl, the matching level between experimental AC-TEM images and TEM image simulations based on DFT-relaxed CuCl/MoS_2 models, geometric relationship between type-I and type-II heteroepitaxy, stacking orientations of thick cubic CuCl on monolayer MoS_2 (PDF)

AUTHOR INFORMATION

Corresponding Author

*E-mail: jamie.warner@materials.ox.ac.uk.

ORCID

Shanshan Wang: 0000-0003-3750-6737
Junying Zhang: 0000-0002-4860-8774
Jamie H. Warner: 0000-0002-1271-2019

Notes

The authors declare no competing financial interest.

ACKNOWLEDGMENTS

J.H.W. thanks the Royal Society for support. S.W. thanks the China Scholarship Council for support. H.L. thanks the support from ExxonMobil under the MIT Energy Initiative (Grant EM09079). This research used resources of the National Energy Research Scientific Computing Center, a DOE Office of Science User Facility supported by the Office of Science of the U.S. Department of Energy under Contract No. DE-AC02-05CH11231.

REFERENCES

(1) Kim, K. K.; Hsu, A.; Jia, X.; Kim, S. M.; Shi, Y.; Hofmann, M.; Nezich, D.; Rodriguez-Nieva, J. F.; Dresselhaus, M.; Palacios, T.; Kong, J. Synthesis of Monolayer Hexagonal Boron Nitride on Cu Foil Using Chemical Vapor Deposition. *Nano Lett.* **2012**, *12*, 161−166.

(2) Kim, S. M.; Hsu, A.; Park, M. H.; Chae, S. H.; Yun, S. J.; Lee, J. S.; Cho, D.-H.; Fang, W.; Lee, C.; Palacios, T.; Dresselhaus, M.; Kim, K. K.; Lee, Y. H.; Kong, J. Synthesis of Large-Area Multilayer Hexagonal Boron Nitride for High Material Performance. *Nat. Commun.* **2015**, *6*, 8662.

(3) Kang, K.; Xie, S.; Huang, L.; Han, Y.; Huang, P. Y.; Mak, K. F.; Kim, C.-J.; Muller, D.; Park, J. High-Mobility Three-Atom-Thick Semiconducting Films with Wafer-Scale Homogeneity. *Nature* **2015**, *520*, 656−660.

(4) Najmaei, S.; Liu, Z.; Zhou, W.; Zou, X.; Shi, G.; Lei, S.; Yakobson, B. I.; Idrobo, J.-C.; Ajayan, P. M.; Lou, J. Vapour Phase Growth and Grain Boundary Structure of Molybdenum Disulphide Atomic Layers. *Nat. Mater.* **2013**, *12*, 754−759.

(5) van der Zande, A. M.; Huang, P. Y.; Chenet, D. A.; Berkelbach, T. C.; You, Y.; Lee, G.-H.; Heinz, T. F.; Reichman, D. R.; Muller, D. A.; Hone, J. C. Grains and Grain Boundaries in Highly Crystalline Monolayer Molybdenum Disulphide. *Nat. Mater.* **2013**, *12*, 554−561.

(6) Geim, A. K.; Grigorieva, I. V. Van Der Waals Heterostructures. *Nature* **2013**, *499*, 419−425.

(7) Liu, Z.; Song, L.; Zhao, S.; Huang, J.; Ma, L.; Zhang, J.; Lou, J.; Ajayan, P. M. Direct Growth of Graphene/Hexagonal Boron Nitride Stacked Layers. *Nano Lett.* **2011**, *11*, 2032−2037.

(8) Meng, J. H.; Zhang, X. W.; Wang, H. L.; Ren, X. B.; Jin, C. H.; Yin, Z. G.; Liu, X.; Liu, H. Synthesis of In-Plane and Stacked Graphene/Hexagonal Boron Nitride Heterostructures by Combining with Ion Beam Sputtering Deposition and Chemical Vapor Deposition. *Nanoscale* **2015**, *7*, 16046−16053.

DOI: 10.1021/acsnano.7b02838
ACS Nano 2017, 11, 6404−6415

(9) Shi, Y.; Zhou, W.; Lu, A.-Y.; Fang, W.; Lee, Y.-H.; Hsu, A. L.; Kim, S. M.; Kim, K. K.; Yang, H. Y.; Li, L.-J.; Idrobo, J.-C.; Kong, J. Van Der Waals Epitaxy of MoS_2 Layers Using Graphene as Growth Templates. *Nano Lett.* **2012**, *12*, 2784−2791.
(10) Shi, J.; Liu, M.; Wen, J.; Ren, X.; Zhou, X.; Ji, Q.; Ma, D.; Zhang, Y.; Jin, C.; Chen, H.; Deng, S.; Xu, N.; Liu, Z.; Zhang, Y. All Chemical Vapor Deposition Synthesis and Intrinsic Bandgap Observation of MoS_2/Graphene Heterostructures. *Adv. Mater.* **2015**, *27*, 7086−7092.
(11) Latorre-Sánchez, M.; Esteve-Adell, I.; Primo, A.; García, H. Innovative Preparation of MoS_2-Graphene Heterostructures Based on Alginate Containing $(NH_4)_2MoS_4$ and Their Photocatalytic Activity for H2 Generation. *Carbon* **2015**, *81*, 587−596.
(12) Wang, S.; Wang, X.; Warner, J. H. All Chemical Vapor Deposition Growth of MoS_2:h-BN Vertical van Der Waals Heterostructures. *ACS Nano* **2015**, *9*, 5246−5254.
(13) Fu, L.; Sun, Y.; Wu, N.; Mendes, R. G.; Chen, L.; Xu, Z.; Zhang, T.; Rümmeli, M. H.; Rellinghaus, B.; Pohl, D.; Zhuang, L.; Fu, L. Direct Growth of MoS_2/h-BN Heterostructures *via* a Sulfide-Resistant Alloy. *ACS Nano* **2016**, *10*, 2063−2070.
(14) Gong, Y.; Lin, J.; Wang, X.; Shi, G.; Lei, S.; Lin, Z.; Zou, X.; Ye, G.; Vajtai, R.; Yakobson, B. I.; Terrones, H.; Terrones, M.; Tay, B. K.; Lou, J.; Pantelides, S. T.; Liu, Z.; Zhou, W.; Ajayan, P. M. Vertical and in-Plane Heterostructures from WS_2/MoS_2 Monolayers. *Nat. Mater.* **2014**, *13*, 1135−1142.
(15) Woods, J. M.; Jung, Y.; Xie, Y.; Liu, W.; Liu, Y.; Wang, H.; Cha, J. J. One-Step Synthesis of MoS_2/WS_2 Layered Heterostructures and Catalytic Activity of Defective Transition Metal Dichalcogenide Films. *ACS Nano* **2016**, *10*, 2004−2009.
(16) Zhang, J.; Wang, J.; Chen, P.; Sun, Y.; Wu, S.; Jia, Z.; Lu, X.; Yu, H.; Chen, W.; Zhu, J.; Xie, G.; Yang, R.; Shi, D.; Xu, X.; Xiang, J.; Liu, K.; Zhang, G. Observation of Strong Interlayer Coupling in MoS_2/WS_2 Heterostructures. *Adv. Mater.* **2016**, *28*, 1950−1956.
(17) Yang, W.; Chen, G.; Shi, Z.; Liu, C.-C; Zhang, L.; Xie, G.; Cheng, M.; Wang, D.; Yang, R.; Shi, D.; Watanabe, K.; Taniguchi, T.; Yao, Y.; Zhang, Y.; Zhang, G. Epitaxial Growth of Single-Domain Graphene on Hexagonal Boron Nitride. *Nat. Mater.* **2013**, *12*, 792−797.
(18) Yan, A.; Velasco, J.; Kahn, S.; Watanabe, K.; Taniguchi, T.; Wang, F.; Crommie, M. F.; Zettl, A. Direct Growth of Single- and Few-Layer MoS_2 on H-BN with Preferred Relative Rotation Angles. *Nano Lett.* **2015**, *15*, 6324−6331.
(19) Lin, Y.; Chang, C. S.; Ghosh, R. K.; Li, J.; Zhu, H.; Diaconescu, B.; Ohta, T.; Peng, X.; Lu, N.; Kim, M. J.; Robinson, J. T.; Wallace, R. M.; Mayer, T. S.; Datta, S.; Li, L.-J.; Robinson, J. A. Atomically Thin Heterostructures Based on Single-Layer Tungsten Diselenide and Graphene. *Nano Lett.* **2014**, *14*, 6936−6941.
(20) Miwa, J. A.; Dendzik, M.; Grønborg, S. S.; Bianchi, M.; Lauritsen, J. V.; Hofmann, P.; Ulstrup, S. Van Der Waals Epitaxy of Two-Dimensional MoS_2 Graphene Heterostructures in Ultrahigh Vacuum. *ACS Nano* **2015**, *9*, 6502−6510.
(21) Liu, X.; Balla, I.; Bergeron, H.; Campbell, G. P.; Bedzyk, M. J.; Hersam, M. C. Rotationally Commensurate Growth of MoS_2 on Epitaxial Graphene. *ACS Nano* **2016**, *10*, 1067−1075.
(22) Novoselov, K. S.; Mishchenko, A.; Carvalho, A.; Castro Neto, A. H. 2D Materials and van Der Waals Heterostructures. *Science* **2016**, *353*, aac9439.
(23) Chen, Q.; He, K.; Robertson, A. W.; Kirkland, A. I.; Warner, J. H. Atomic Structure and Dynamics of Epitaxial 2D Crystalline Gold on Graphene at Elevated Temperatures. *ACS Nano* **2016**, *10*, 10418−10427.
(24) Al Balushi, Z. Y.; Wang, K.; Ghosh, R. K.; Vilá, R. A.; Eichfeld, S. M.; Caldwell, J. D.; Qin, X.; Lin, Y.-C.; DeSario, P. A.; Stone, G.; Subramanian, S.; Paul, D. F.; Wallace, R. M.; Datta, S.; Redwing, J. M.; Robinson, J. A. Two-Dimensional Gallium Nitride Realized *via* Graphene Encapsulation. *Nat. Mater.* **2016**, *15*, 1166−1171.
(25) Zhao, J.; Deng, Q.; Bachmatiuk, A.; Sandeep, G.; Popov, A.; Eckert, J.; Rümmeli, M. H. Free-Standing Single-Atom-Thick Iron Membranes Suspended in Graphene Pores. *Science* **2014**, *343*, 1228−1232.
(26) Quang, H. T.; Bachmatiuk, A.; Dianat, A.; Ortmann, F.; Zhao, J.; Warner, J. H.; Eckert, J.; Cunniberti, G.; Rümmeli, M. H. *In Situ* Observations of Free-Standing ZnO Membranes. *ACS Nano* **2015**, *9*, 11408−11413.
(27) Madelung, O. *Semiconductors: Data Handbook*; Springer: Berlin, 2003; pp 911−914.
(28) Nakayama, M.; Ichida, H.; Nishimura, H. Bound-Biexciton Photoluminescence in CuCl Thin Films Grown by Vacuum Deposition. *J. Phys.: Condens. Matter* **1999**, *11*, 7653−7662.
(29) Robertson, A. W.; Montanari, B.; He, K.; Allen, C. S.; Wu, Y. a.; Harrison, N. M.; Kirkland, A. I.; Warner, J. H. Structural Reconstruction of the Graphene Monovacancy. *ACS Nano* **2013**, *7*, 4495−4502.
(30) Wang, S.; Rong, Y.; Fan, Y.; Pacios, M.; Bhaskaran, H.; He, K.; Warner, J. H. Shape Evolution of Monolayer MoS_2 Crystals Grown by Chemical Vapor Deposition. *Chem. Mater.* **2014**, *26*, 6371−6379.
(31) Wang, S.; Lee, G.-D.; Lee, S.; Yoon, E.; Warner, J. H. Detailed Atomic Reconstruction of Extended Line Defects in Monolayer MoS_2. *ACS Nano* **2016**, *10*, 5419−5430.
(32) Rasool, H. I.; Ophus, C.; Zhang, Z.; Crommie, M. F.; Yakobson, B. I.; Zettl, A. Conserved Atomic Bonding Sequences and Strain Organization of Graphene Grain Boundaries. *Nano Lett.* **2014**, *14*, 7057−7063.
(33) Chen, Q.; Robertson, A. W.; He, K.; Gong, C.; Yoon, E.; Lee, G.; Warner, J. H. Atomic Level Distributed Strain within Rotations. *ACS Nano* **2015**, *9*, 8599−8608.
(34) Warner, J. H.; Young, N. P.; Kirkland, A. I.; Briggs, G. A. D. Resolving Strain in Carbon Nanotubes at the Atomic Level. *Nat. Mater.* **2011**, *10*, 958−962.
(35) Kresse, G.; Furthmüller, J. Efficient Iterative Schemes for *Ab Initio* Total-Energy Calculations Using a Plane-Wave Basis Set. *Phys. Rev. B: Condens. Matter Mater. Phys.* **1996**, *54*, 11169−11186.
(36) Blochl, P. E. Projector Augmented-Wave Method. *Phys. Rev. B: Condens. Matter Mater. Phys.* **1994**, *50*, 17953−17979.
(37) Perdew, J. P.; Burke, K.; Ernzerhof, M. Generalized Gradient Approximation Made Simple. *Phys. Rev. Lett.* **1996**, *77*, 3865−3868.
(38) Grimme, S.; Antony, J.; Ehrlich, S.; Krieg, H. A Consistent and Accurate *Ab Initio* Parametrization of Density Functional Dispersion Correction (DFT-D) for the 94 Elements H-Pu. *J. Chem. Phys.* **2010**, *132*, 154104.
(39) Makov, G.; Payne, M. Periodic Boundary Conditions in *Ab Initio* Calculations. *Phys. Rev. B: Condens. Matter Mater. Phys.* **1995**, *51*, 4014−4022.
(40) Pack, J. D.; Monkhorst, H. J. Special Points for Brillouin-Zone Integrations"—a Reply. *Phys. Rev. B* **1977**, *16*, 1748−1749.
(41) Liechtenstein, A. I.; Anisimov, V. I.; Zaanen, J. Density-Functional Theory and Strong Interactions: Orbital Ordering in Mott-Hubbard Insulators. *Phys. Rev. B: Condens. Matter Mater. Phys.* **1995**, *52*, 5467−5471.
(42) Zhou, B.; Dong, S.; Wang, J.; Zhao, H.; Wu, P. Effects of Enhanced Electronic Correlation on Magnetic Properties of Light Non-Metallic Element (B, C, N, and O)-Doped CuCl: A First-Principles Study. *Phys. Lett. A* **2014**, *378*, 3001−3005.

DOI: 10.1021/acsnano.7b02838
ACS Nano 2017, 11, 6404−6415